Superconductivity of Topological Surface States and Strong Proximity Effect in Sn 1– x Pb x Te–Pb Heterostructures

Superconductivity of Topological Surface States and Strong Proximity Effect in $Sn_{1-x}Pb_xTe$-Pb Heterostructures

Hao Yang, Yao-Yi Li, Teng-Teng Liu, Huan-Yi Xue, Dan-Dan Guan, Shi-Yong Wang, Hao Zheng, Can-Hua Liu, Liang Fu, and Jin-Feng Jia**

Hao Yang, Prof. Yao-Yi Li, Teng-Teng Liu, Huan-Yi Xue, Dr. Dan-Dan Guan, Prof. Shi-Yong Wang, Prof. Hao Zheng, Prof. Can-Hua Liu, Prof. Jin-Feng Jia

Key Laboratory of Artificial Structures and Quantum Control (Ministry of Education), Shenyang National Laboratory for Materials Science, School of Physics and Astronomy, Shanghai Jiao Tong University, 800 Dongchuan Road, Shanghai 200240, China

E-mail: yaoyili@sjtu.edu.cn; jfjia@sjtu.edu.cn

Prof. Liang Fu

Department of Physics, Massachusetts Institute of Technology, Cambridge, Massachusetts 02139, USA

Prof. Yao-Yi Li, Dr. Dan-Dan Guan, Prof. Shi-Yong Wang, Prof. Hao Zheng, Prof. Can-Hua Liu, Prof. Jin-Feng Jia

Collaborative Innovation Center of Advanced Microstructures, Nanjing 210093, China

Prof. Yao-Yi Li, Dr. Dan-Dan Guan, Prof. Shi-Yong Wang, Prof. Hao Zheng, Prof. Can-Hua Liu, Prof. Jin-Feng Jia

Tsung-Dao Lee Institute, Shanghai 200240, China

This is the author manuscript accepted for publication and has undergone full peer review but has not been through the copyediting, typesetting, pagination and proofreading process, which may lead to differences between this version and the Version of Record. Please cite this article as doi: 10.1002/adma.201905582.

Keywords: topological crystalline insulator, superconductivity, toplogical surface states, proximity effect, heterostructure

Supereonducting topological crystalline insulators are expected to form a new type of topological superconductors to host Majorana zero modes under the protection of lattice symmetries. The bulk superconductivity of topological crystalline insulators has been induced through chemical doping and proximity effect. However, only conventional full gaps are observed, so the existence of topological superconductivity in topological crystalline insulators is still controversial. Here, we report the successful fabrication of atomically flat lateral and vertical $Sn_{1-x}Pb_xTe$-Pb heterostructures by molecular beam epitaxy. The superconductivity of the $Sn_{1-x}Pb_xTe$-Pb heterostructures can be directly investigated by scanning tunneling spectroscopy. Unconventional peak-dip-hump gap features and fourfold symmetric quasiparticle interference patterns taken at the zero energy support the presence of the topological superconductivity in superconducting $Sn_{1-x}Pb_xTe$. Strong superconducting proximity effect and easy preparation of various constructions between $Sn_{1-x}Pb_xTe$ and Pb make the heterostructures to be a promising candidate for topological superconducting devices to detect and manipulate Majorana zero modes in the future.

A topological superconductor (TSC) is characterized by having a pairing gap in the bulk and gapless Andreev bound states at its boundary, which is topologically distinct from a conventional superconductor (SC).[1,2] TSCs contain Majorana zero modes (MZMs) which obey non-Abelian statistics,[3-5] thus exhibiting great potential applications in fault-tolerant topological quantum computing.[6-8] After the realization of topological insulators (TIs),[1,9,10] the search for TSCs in real materials has already been a very hot topic in condensed matter physics. Natural TSCs are rarely found, but topological superconductivity can be induced in TIs through chemical doping and superconducting proximity effect. Bulk superconductivity of doped TIs such as Cu,[11,12] Sr,[13,14] Nb[15,16] doped Bi_2Se_3 have been discovered. The superconducting doped TI is considered as TSC,[17,18] but scanning tunneling microscopy and spectroscopy (STM/STS) experiments show conventional full BCS-like *s*-wave gaps without any in-gap states.[19,20] Further calculation suggests that the U-shaped STS spectrum in $Cu_xBi_2Se_3$ is related to the cylindrical shape of the Fermi surface.[21,22] For proximity induced superconductivity in TIs, it has been theoretically proposed that combining a conventional *s*-

wave SC with a TI results in a topological p_x+ip_y superconductivity that hosts MZMs in vortices.[8] The TI/SC heterostructure has been successfully prepared by the epitaxial growth of TI films on superconducting $NbSe_2$.[23,24] The experimental evidences of MZMs in vortices are found in the $Bi_2Te_3/NbSe_2$ heterostructure.[25,26]

Topological crystalline insulators (TCIs) are topologically nontrivial states of matter that the gapless surface states are protected by crystalline symmetry instead of time-reversal symmetry.[27,28] The first class of TCIs has been recently predicted[29] and verified[30-32] in the SnTe-type IV-VI semiconductors with a rock-salt crystal structure. Superconducting TCIs are expected to form a new type of TSCs that multiple MZMs bound to a single vortex may be supported under the protection of lattice symmetries.[33,34] The bulk superconductivity of TCIs has been induced through chemical doping[35] and proximity effect.[36,37] However, STM experiments still display the conventional full gaps in the superconducting TCI,[38] so the existence of topological superconductivity in TCIs remains controversial.

In this work, we fabricated atomically flat lateral and vertical $Sn_{1-x}Pb_xTe$-Pb heterostructures by molecular beam epitaxy (MBE). The superconductivity of the $Sn_{1-x}Pb_xTe$-Pb heterostructures can be directly investigated by *in situ* low temperature STM/STS. The superconducting proximity effect in the heterostructures is unexpectedly strong even at 4.2 K. The features of the tunneling spectra taken on superconducting $Sn_{1-x}Pb_xTe$ show a peak-dip-hump character rather than the peak-shoulder character seen in conventional SCs such as Pb, which is in agreement with the existence of topological odd-parity pairing.[21,39] The unconventional feature in $Sn_{1-x}Pb_xTe$ is still clearly visible above 6.5 K. Quasiparticle interference (QPI) patterns taken at the zero energy in the superconducting gap of $Sn_{1-x}Pb_xTe$ show a fourfold symmetry, indicating the presence of gapless in-gap states. Although the superconducting transition temperature (T_c) of Pb is close to that of $NbSe_2$,

the decay of the proximity-induced superconducting gap in $Sn_{1-x}Pb_xTe$/Pb is much slower than that in $Bi_2Te_3/NbSe_2$. The superconducting TCI is predicted to be a new class of TSC supporting MZMs protected by lattice symmetries.[33,34] Our results suggest that the $Sn_{1-x}Pb_xTe$-Pb heterostructures have great potential application in topological superconducting devices to detect and manipulate MZMs in the future.

The STM images of the lateral and vertical $Sn_{1-x}Pb_xTe$-Pb heterostructures are shown in **Figure 1**. Pb islands were firstly prepared on graphene/SiC substrates at room temperature. SnTe was then deposited on the Pb islands. The Pb islands can keep flat-topped even when the annealing temperature is raised to 200 °C. When the substrate temperature is higher than 90 °C, it's strange that SnTe islands grow not on top of but beside the Pb islands (Figure 1a). The (001) surface of pure SnTe displays a high density of Sn vacancies (Figure S1a, Supporting Information).[40] However, the atomically resolved STM image taken on a SnTe island shows a (001) surface of $Sn_{1-x}Pb_xTe$ (Figure 1b), which indicates that some Pb atoms diffuse into the SnTe island grown beside a Pb island. Figure 1c is the atomic structure on top of a Pb island. The clean Pb (111) surface is preserved in despite of the lateral growth of a SnTe island. When the substrate temperature is lower than 90 °C, most of the Pb islands are covered by SnTe (Figure 1d). The SnTe-covered Pb islands have monoatomic steps (~ 0.32 nm) (Figure 1d) and a square lattice on top (Figure S1b, Supporting Information). The substrate temperature dependent growth mode of SnTe on Pb is due to the kinetic mechanism.[41] When the substrate temperature is higher than 90 °C, the mobility of SnTe on Pb is large, so that the adatoms escape from the top of the Pb island. The growth mode is step-flow growth. When the substrate temperature is lower than 90 °C, the mobility of SnTe on Pb is reduced, then SnTe nucleate and grow on top of the Pb island. Since the surface energy of SnTe (001) (9.7 meV/Å^2)[42] is smaller than that of Pb (111) (27.5 meV/Å^2),[43] the growth mode becomes 2D growth.

Compared with pure SnTe (001)/graphene, there are a lot of bright spots on SnTe (001)/Pb (Figures S1a,b, Supporting Information), which indicates that some Pb atoms will also diffuse into SnTe grown on Pb islands below 90 °C. For Pb-Sn-Te ternary system, there doesn't exists PbTe but $Sn_{1-x}Pb_xTe$ phase even under Pb-rich environment.[44] To determine the concentration of Pb, $Sn_{1-x}Pb_xTe$ films were prepared on graphene/SiC by the co-deposition of Pb and SnTe for comparison (Figures S1c,d, Supporting Information). The density of bright spots increases with the increase of the Pb/SnTe flux ratio, which indicates the bright spots should be Pb atoms. In addition, first-principles calculations show that Sn 5*p* states are dominant for conduction bands of SnTe, whereas Te 5*p* states are dominant for valence bands.[45] Then, the atomically resolved STM images of $Sn_{1-x}Pb_xTe$ at positive sample biases should correspond to the Sn sublattice.[40] Alloying with Pb can cause *n* doping by lowering the conduction band minimum (CBM),[46] which give rise to an increase in the density of states (DOS) near the bottom of the conduction band, so Pb is brighter than Sn at positive sample biases when a Pb atom occupies a Sn site. The concentration of Pb can be determined by counting the bright spots in an atomically resolved STM image. Figure 1b and Figure S1b in the Supporting Information exhibit 18.5% and 2.7% Pb respectively, which are much smaller than the critical value (75% Pb) for topological-to-trivial phase transition.[32,47] Tuning the substrate temperature, both lateral and vertical $Sn_{1-x}Pb_xTe$-Pb heterostructures can be prepared (Figures 1e,f). In addition, the $Sn_{1-x}Pb_xTe$ islands are not covered by Pb islands or clusters, so the intrinsic superconductivity of $Sn_{1-x}Pb_xTe$ can be directly detected by STM/STS.

Figure 2a shows a lateral heterostructure consisting of a 16.3 nm (57 ML) thick Pb island and a 9.7 nm (31 ML) thick $Sn_{1-x}Pb_xTe$ island. Both islands have large-scale atomically flat terraces. The boundary between the Pb island and the $Sn_{1-x}Pb_xTe$ island is very straight. A series of d*I*/d*V* spectra (Figure 2b) were measured using a Pb-coated superconducting tip at 4.2 K along the black dashed

line shown in Figure 2a. The superconducting tip can enhance the spectra resolution[48,49] and was prepared *in situ* by indenting a W tip into a Pb island. All the d*I*/d*V* spectra show two sharp coherence peaks, indicating the $Sn_{1-x}Pb_xTe$ island shown in Figure 2a are superconducting. The energies of the two sharp coherence peaks in the d*I*/d*V* spectra correspond to $\pm(\Delta_{Pb}+\Delta_{Sn1-xPbxTe})$. $\pm\Delta_{Pb}$ and $\pm\Delta_{Sn1-xPbxTe}$ are the energies of the two sharp coherence peaks in the DOS of superconducting Pb and $Sn_{1-x}Pb_xTe$ respectively, which can be extracted from the d*I*/d*V* spectra taken on Pb and $Sn_{1-x}Pb_xTe$ islands. The spatial evolution of $\Delta_{Sn1-xPbxTe}$ as a function of distance is shown in Figure 2c. $\Delta_{Sn1-xPbxTe}$ taken on the $Sn_{1-x}Pb_xTe$ island decreases from 0.88 meV at the position A1 of ~10 nm away from the Pb island edge to 0.54 meV at the position A2 of ~130 nm away from the Pb island edge. The solid blue line in Figure 2c is an exponential fit by $y = A*\exp(-x/L)+C$, with a decay length L as large as 362 nm. For the Pb/Si (111) system, at 4.2K, the superconducting gap taken at 30 nm away from the Pb island edge is hard to be distinguished.[50] Even at 1.8 K, the decay length of the proximity induced superconducting gap is only ~75 nm.[51] Therefore, the decay length in the $Sn_{1-x}Pb_xTe$-Pb lateral heterostructure is much longer than that in the Pb/Si (111) system.

Figure 2d shows a vertical $Sn_{1-x}Pb_xTe$-Pb heterostructure with a ~15 nm (~48 ML) thick $Sn_{1-x}Pb_xTe$ island grown on Pb. There are a lot of monoatomic steps (~0.32 nm) on top of the $Sn_{1-x}Pb_xTe$ island. A series of d*I*/d*V* spectra taken along the black dashed line shown in Figure 2d are plotted into Figure 2e. All the d*I*/d*V* spectra show two very sharp peaks. The spatial evolution of $\Delta_{Sn1-xPbxTe}$ as a function of the distance is shown in Figure 2f. $\Delta_{Sn1-xPbxTe}$ has little change between 1.00 meV and 1.18 meV, which is 76-90 % of Δ_{Pb} (1.31 meV). For the lateral heterostructure shown in Figure 2a, $\Delta_{Sn1-xPbxTe}$ at the distance of ~15nm away from the Pb island edge is 50-60 % of Δ_{Pb} (1.34 meV). If there exists Pb underneath the $Sn_{1-x}Pb_xTe$ region of the lateral heterostructure, the thickness of $Sn_{1-x}Pb_xTe$ in Figure 2a should be smaller than 10 nm. Then, the $\Delta_{Sn1-xPbxTe}$ in the region from 30 nm to

120 nm shown in Figure 2c should be larger than 1.18 meV. In fact, $\Delta_{Sn1-xPbxTe}$ in the region from 30 nm to 120 nm shown in Figure 2c is only 0.51-0.72 meV. Therefore, the measurement of $\Delta_{Sn1-xPbxTe}$ in the vertical heterostructure shown in Figure 2f indicates that there doesn't exist Pb underneath the $Sn_{1-x}Pb_xTe$ region for the lateral heterostructure, which supports the schematic diagram of the lateral $Sn_{1-x}Pb_xTe$-Pb heterostructure shown in Figure 1e. Comparison of the spatial evolutions shown in Figures 2c,f indicates that $\Delta_{Sn1-xPbxTe}$ in the vertical heterostructure decays obviously slower than that in the lateral heterostructure. For the vertical $Bi_2Te_3/NbSe_2$ heterostructure,[24] the superconducting gap taken on the 11 nm thick Bi_2Te_3 film is only ~20 % of that taken on the $NbSe_2$ substrate at 0.4 K. Therefore, the results shown in Figure 2 exhibit that the proximity effects in the $Sn_{1-x}Pb_xTe$-Pb heterostructures are unexpectedly strong even at higher temperature 4.2 K.

Comparison of the gap features of Pb and $Sn_{1-x}Pb_xTe$ reveals that $Sn_{1-x}Pb_xTe$ possesses unconventional superconductivity. **Figure 3**a shows another lateral $Sn_{1-x}Pb_xTe$ heterostructure. The d*I*/d*V* spectrum taken on the Pb island with a Pb-coated superconducting tip is shown in Figure 3b. Outside the two sharp coherence peaks at ±2.69 mV, there are two broad shoulders due to strong electron-phonon coupling.[52] The d*I*/d*V* spectrum is simulated with the S-I-S tunneling model (Supplementary Note, Supporting Information). The corresponding sample DOS of Pb is shown in Figure 3c. Figure 3d is the d*I*/d*V* spectrum taken on the $Sn_{1-x}Pb_xTe$ island. The small peaks around the zero bias voltage shown in Figures 3b,d are induced by the tunneling of thermal excited states.[48] It's strange that there are two dips at ±2.54 meV outside the two large coherence peaks at ±1.95 meV. If the sample DOS of $Sn_{1-x}Pb_xTe$ is BCS-like, the simulated curve in Figure 3d fits the d*I*/d*V* spectrum well between the two sharp coherence peaks, but it fails to represent the dip feature. We note the features of the d*I*/d*V* spectrum taken on $Sn_{1-x}Pb_xTe$ are very similar to those of magnetic molecules adsorbed on SC surfaces,[48,53] so the d*I*/d*V* spectrum is simulated with a modified sample DOS

(Figure 3e and Supplementary Note, Supporting Information). The simulations reproduce the peak and dip features very well. The corresponding sample DOS of $Sn_{1-x}Pb_xTe$ in Figure 3f are obviously different from the BCS-like DOS of Pb in Figure 3c.

For magnetic molecules adsorbed on SC surfaces, the dip features of the d*I*/d*V* spectra taken on the magnetic molecules correspond to the bulk superconducting gap of the SC substrates.[48,53] The peaks between the two dips are in-gap YSR states within the bulk superconducting gap. Moreover, theoretical calculations demonstrate that when the superconducting TIs and TCIs possess topological superconductivity, their DOS also have dip features,[21,39] the energy positions of which are close to the bulk superconducting gap. Our temperature dependent experiments show that the peak and dip features of $Sn_{1-x}Pb_xTe$ are still clearly visible above 6.5 K (Figure S2, Supporting Information), so the T_c of $Sn_{1-x}Pb_xTe$ should be above 6.5 K in the $Sn_{1-x}Pb_xTe$-Pb heterostructures, which is even higher than the maximum T_c of In doped $Sn_{1-x}Pb_xTe$ (T_c = 4.7 K).[54] However, not the energy (Δ_{s1} = 0.72 meV) of the sharp coherence peaks but that (Δ_{s2} = 1.20 meV) of the hump feature in Figure 3e is larger than the bulk superconducting gap (0.90 meV) of In doped $Pb_{0.5}Sn_{0.5}Te$.[38] Therefore, the dips in the d*I*/d*V* spectra taken on $Sn_{1-x}Pb_xTe$ should correspond to the bulk superconducting gap edges, and the coherence peaks between the two dips should be in-gap states.

The dip feature can be observed in both lateral and vertical $Sn_{1-x}Pb_xTe$-Pb heterostructures. For the lateral heterostructure, the dip feature appears at the distance larger than ~15 nm (Figure S3, Supporting Information). When the position is very close to the Pb island edge, the dip feature will be covered by the coherence peaks. For the vertical heterostructure, since the thickness of $Sn_{1-x}Pb_xTe$ is ~15 nm, the dip feature is weak, but the d*I*/d*V* spectra have similar features with those taken on the lateral heterostructure at the distance of ~15 nm to the Pb island edge (Figure S4, Supporting Information).

The dip feature cannot be resolved by normal tips at 4.2 K. Both Pb and $Sn_{1-x}Pb_xTe$ just exhibit a superconducting gap with two very broad peaks (Figure S5, Supporting Information). For a normal tip, the energy resolution in STS experiments is limited by the Fermi-Dirac distribution. The thermal broadening (~$3.2k_BT$) is estimated to be 1.2 meV at 4.2 K.[55] For a superconducting tip, the energy resolution is limited by the BCS-like DOS of the superconducting tip. The energy resolution can be less than 0.3 meV at 4.2 K.[48] The resolution can be further improved with the reduction of the electronic noise in the instrument. In our case, the instrumental broadening is 0.19-0.48 meV at 4.2 K, which is obtained by fitting the d*I*/d*V* spectra taken on Pb (Figure S6, Supporting Information). The smaller instrumental broadening, the sharper the peak and dip features will be. Because of the higher energy resolution, it's very necessary to use the superconducting tip to find out the unconventional superconductivity of $Sn_{1-x}Pb_xTe$.

In order to reveal the in-gap structure, the Fourier-transform (FT) STS measurements were performed on $Sn_{1-x}Pb_xTe$ (001). **Figure 4**a is a typical d*I*/d*V* spectrum taken on the $Sn_{1-x}Pb_xTe$ region of a lateral heterostructure. The spatial evolution of d*I*/d*V* spectra taken along a line shows that the minimum of the dI/dV spectrum taken near the Pb island edge is at ~0.2 eV below E_F, whereas the minimum at the distance larger than 50 nm away from the Pb island edge is at ~0.1 eV below E_F (Figure S7, Supporting Information). The sharp coherence peaks are still clearly visible at the distance of ~120 nm far from the Pb island edge (Figure S8, Supporting Information). d*I*/d*V* maps at bias voltages from 0.5 V to -0.5 V (Figure S9, Supporting Information) were taken on a 50×50 nm^2 area (marked by the green square shown in Figure S7, Supporting Information). For a better signal-to-noise ratio, the raw QPI patterns obtained by FT-d*I*/d*V* maps are four-fold symmetrized by rotation and reflection averaging along high symmetry directions (Figure 4b and Figure S10, Supporting Information). Figure 4c is the corresponding schematic Fermi surface of $Sn_{1-x}Pb_xTe$ (001) in the

surface Brillouin zone (SBZ). There are three main features in the symmetrized QPI patterns: the Bragg points and the patterns induced by inter-pocket ($\boldsymbol{q_1}$) and intra-pocket ($\boldsymbol{q_2}$) scattering wavevectors. When the bias voltage changes from 0.5 V to -0.5 V, the shape of the pattern around $\boldsymbol{q_1}$ undergoes a transition from quasi-circular to dot-like to quasi-circular again, which is consistent with the evolution of QPI patterns induced by the topological surface states of $Pb_{1-x}Sn_xSe$.[56,57] The dot-like pattern around $\boldsymbol{q_1}$ appears at the bias voltage of -0.1 V, indicating that the energy position (E_D) of Dirac points should be located around 0.1 eV below E_F. The minimum of the d*I*/d*V* spectrum taken on $Sn_{1-x}Pb_xTe$ (001) thus corresponds to E_D, which is consistent with other QPI measurements of SnTe-type TCIs.[40,56,57]

Previous ARPES experiments show that the Dirac points of $Sn_{1-x}Pb_xTe$ (001) are close to but still above E_F even when the concentration of Pb reaches 60-70%.[32,47] Transport experiments exhibit hole concentration from 10^{17} to 10^{20} cm^{-3} in $Sn_{1-x}Pb_xTe$ films.[58] It's difficult to obtain n-type SnTe with Pb alloying. Nevertheless, earlier studies in $Sn_{1-x}Pb_xTe$-Pb[59-61] and $Sn_{1-x}Pb_xTe$-Insulator-Pb[62] junctions exhibit downward band bending of p-type $Sn_{1-x}Pb_xTe$ due to the work function of Pb smaller than the electron affinity of $Sn_{1-x}Pb_xTe$. Our STM/STS measurements show that for the lateral $Sn_{1-x}Pb_xTe$-Pb heterostructure grown at 150 °C, the concentration of Pb at the distance smaller than 50 nm away from the Pb island edge is below 25%, whereas it decreases to no more than 5% at the distance larger than 100 nm (Figure S11, Supporting Information). It's unexpected that the corresponding minima of the d*I*/d*V* spectra are [-0.20eV, -0.10eV] and [-0.08eV, -0.04eV] respectively. For pure SnTe, E_D is 0.35 eV above E_F.[40] It's impossible for Pb alloying but band bending near interface to force the Dirac points of $Sn_{1-x}Pb_xTe$ to shift below E_F. The measured bulk band gap of $Sn_{1-x}Pb_xTe$ with 5-20% Pb at 4.2K is 0.20-0.25 eV.[63,64] Since E_D near the Pb island edge is ~0.2 eV below E_F (Figures S7 and S11, Supporting Information), the CBM should be ~0.1 eV below E_F. Then,

the energy diagram of the semiconductor-metal contact with an inversion layer is applicable for the lateral $Sn_{1-x}Pb_xTe$-Pb heterostructure (Figure 4d). At the distance of ~100 nm away from the Pb island edge, E_D is ~0.05 eV below E_F (Figure S11, Supporting Information), the Fermi level should lie within the bulk gap of $Sn_{1-x}Pb_xTe$. Hence, the width of the region with the Dirac points close to E_F is estimated to be several hundred nanometers. The downward band bending can tune Dirac points of $Sn_{1-x}Pb_xTe$ close to E_F, which is very crucial for observing superconductivity induced by topological surface states. If Dirac points are far away from the Fermi level, such as Cu-doped Bi_2Se_3 (E_D ~ -0.5 eV)[65] and In-doped SnTe (E_D > 0.5 eV),[66] the bulk states are dominant around E_F. As a result, only conventional superconductivity is observed.

Figure 5a shows the symmetrized QPI patterns taken at the same area in Figure 4 close to E_F at 4.2 K. Since the Pb-coated tip has a superconducting gap Δ_t = 1.32 meV (Figure S8c, Supporting Information), the QPI patterns measured at the bias voltages $V_b = \pm\Delta_t/e$ correspond to those measured at the zero energy within the superconducting gap of $Sn_{1-x}Pb_xTe$. The intensity of the patterns around $\boldsymbol{q_1}$ and $\boldsymbol{q_2}$ taken at the zero energy is very strong (Figure S12, Supporting Information). The pattern around $\boldsymbol{q_2}$ taken at the zero energy is obviously anisotropic, whereas those taken at the larger bias voltages outside the superconducting gap of $Sn_{1-x}Pb_xTe$ become more isotropic. The QPI in the real space induced by the intra-pocket scattering $\boldsymbol{q_2}$ at the zero energy exhibit striped patterns, which are not observed at the bias voltages $|V_b| \geq 20$ mV (Figure 5b and Figure S13, Supporting Information). The striped patterns are not caused by the modulation from the atomic lattice but electronic states (Figure S14, Supporting Information). For the conventional *s*-wave SC Pb, no clear QPI pattern is observed at the zero energy inside the superconducting gap (Figure S15, Supporting Information). In addition, previous QPI measurements have also shown that there is no clear QPI pattern inside the fully opened superconducting gap such as iron-based

SCs,[67,68] β-$PdBi_2$[69] due to the absence of in-gap states. Theoretical calculations have been presented that neither bulk states nor trivial surface states but topological surface states will induce in-gap states.[21,39] Since the bulk superconductivity of $Sn_{1-x}Pb_xTe$ is gapful,[38] the strong QPI pattern measured at the bias voltages $V_b = \pm\Delta_t/e$ within the superconducting gap on the $Sn_{1-x}Pb_xTe$ (001) surface should be induced by not bulk but topological surface states. To further confirm the superconducting gap of $Sn_{1-x}Pb_xTe$ is whether gapful or not, the QPI measurements were taken at the bias voltages from Δ_t/e to $(\Delta_t+\Delta_{s1})/e$, corresponding to the energies from the zero energy to that of the coherence peak within the superconducting gap of $Sn_{1-x}Pb_xTe$ (Figure S16 , Supporting Information). All the QPI images clearly display the patterns induced by $\boldsymbol{q_1}$ and $\boldsymbol{q_2}$. Therefore, our QPI measurements demonstrate that the proximity-induced superconducting $Sn_{1-x}Pb_xTe$ is not a conventional *s*-wave SC and possesses gapless surface states inside the superconducting gap.

In summary, atomically flat lateral and vertical $Sn_{1-x}Pb_xTe$-Pb heterostructures are fabricated on graphitized 6H-SiC (0001) by molecular beam epitaxy. The concentrations of Pb in the heterostructures are smaller than 25%, which are much smaller than the critical value (75% Pb) for topological-to-trivial phase transition.[32,47]. The superconductivity induced by proximity effect in $Sn_{1-x}Pb_xTe$ is unexpectedly robust even above 4.2 K. For the lateral heterostructure, the superconducting coherence peaks are still clearly visible measured at the distance larger than 120 nm from the Pb island edge. The decay length extracted from the spatial evolution of $\Delta_{Sn1-xPbxTe}$ is larger than 200 nm. For the vertical heterostructure, $\Delta_{Sn1-xPbxTe}$ decays obviously slower than that in the lateral heterostructure, indicating the vertical proximity effect is even stronger than the lateral one. The $Sn_{1-x}Pb_xTe$-Pb heterostructures belong to the S-N single-sided junction. For S-N-S double-sided junction, the proximity effect will be further enhanced due to the junction geometry.[50] Our STS measurements demonstrate that the proximity-induced superconducting $Sn_{1-x}Pb_xTe$ is not a

conventional *s*-wave SC. The superconducting gap of $Sn_{1-x}Pb_xTe$ shows a peak-dip-hump character, which is related to the topological nontrivial electronic structures.[21,39] The unconventional feature in $Sn_{1-x}Pb_xTe$ can be distinguished up to 6.5 K, which is even higher than the maximum T_c (4.7 K) of In doped $Sn_{1-x}Pb_xTe$.[54] The numeric simulations and the temperature dependent measurements indicate that the hump feature should correspond to the bulk superconducting gap and the coherence peaks between the two dips should be in-gap states. QPI measurements taken at the bias voltages from Δ_t/e to $(\Delta_t+\Delta_{s1})/e$ within the superconducting gap of $Sn_{1-x}Pb_xTe$ display an anisotropic pattern with a fourfold symmetry, suggesting the present of gapless in-gap states induced by topological surface states. These results support topological superconductivity in proximity-induced superconducting $Sn_{1-x}Pb_xTe$.

Although there are intensive research on topological superconductivity in many systems such as TI/$NbSe_2$,[23-26] Bi2212/TI,[70,71] Bi_2Te_3/FeTe[72] and $FeTe_{1-x}Se_x$,[73-76] the topological surface states in these systems are protected by time-reversal symmetry. In our work, $Sn_{1-x}Pb_xTe$ is a TCI, the topological surface states of which are protected by crystalline symmetry instead of time-reversal symmetry. Superconducting TCIs are expected to form a new type of TSCs.[33,34] In Pb-Bi_2Te_3-Pb double-sided junction, a Josephson supercurrent can flow through the Bi_2Te_3 flake between two superconducting Pb electrodes with a separation distance over several microns below 0.12 K.[77] Recently, anomalous Josephson effects induced by the topological surface states have been reported in Al-$Pb_{0.5}Sn_{0.5}Te$-Al junction.[37,78] Therefore, the $Sn_{1-x}Pb_xTe$-Pb heterostructures have potential applications in large-scale TSC devices and provide a promising platform to detect and manipulate MZMs in a new artificial TSC in the future.

Experimental Section

Sample growth: The experiments were performed in a commercial ultrahigh vacuum low temperature STM system (Unisoku) combined with MBE for film growth. Epitaxial graphene produced by thermal decomposition of 6H-SiC (0001)[79,80] is chosen as the substrate for the growth of $Sn_{1-x}Pb_xTe$-Pb heterostructures. High purity Pb (99.9999%) and SnTe (99.999%) were evaporated from standard Knudsen cells. Pb islands were firstly prepared on graphene/SiC substrates at room temperature. SnTe was then deposited on the Pb islands at elevated temperature. Substrate temperatures higher than 90 °C will lead to the formation of lateral $Sn_{1-x}Pb_xTe$-Pb heterostructures. Substrate temperatures lower than 90 °C will lead to the formation of vertical $Sn_{1-x}Pb_xTe$-Pb heterostructures.

STM/STS measurement: All prepared samples were transferred to a cooling stage kept at 4.2 K by liquid helium. Electrochemically etched polycrystalline tungsten tips were used for *in situ* STM/STS measurements. To increase the energy resolution, the superconducting Pb-coated tip was obtained by embedding the W tip into the Pb island. d*I*/d*V* spectra and d*I*/d*V* maps were acquired using a standard lock-in technique with a small a. c. modulation at 991 Hz. Before STS measurements, the superconducting tip was checked with the d*I*/d*V* spectra taken on Pb islands.

Supporting Information

Supporting Information is available from the Wiley Online Library or from the author.

Acknowledgements

This work is supported by the Ministry of Science and Technology of China (Grants No. 2016YFA0301003, No. 2016YFA0300403), National Natural Science Foundation of China (Grants No. 11861161003, No. 11521404, No. 11634009, No. U1632102, No. 11504230, No. 11674222, No. 11790313, No. 11574202, No. 11674226, No. 11574201, No. 11655002, No. 11874256, No. 11874258 and No. U1632272), the Strategic Priority Research Program of Chinese Academy of Sciences (Grant No. XDB28000000). Y.Y.L. acknowledges support from the Shanghai Jiao Tong University Initiative Scientific Research Program and the National Thousand Young Talents Program.

Received: ((will be filled in by the editorial staff))
Revised: ((will be filled in by the editorial staff))
Published online: ((will be filled in by the editorial staff))

References

[1] X. L. Qi, S. C. Zhang, *Rev. Mod. Phys.* **2011**, 83, 1057.

[2] X. L. Qi, T. L. Hughes, S. Raghu, S. C. Zhang, *Phys. Rev. Lett.* **2009**, 102, 187001.

[3] N. Read, D. Green, *Phys. Rev. B* **2000**, 61, 10267.

[4] D. A. Ivanov, *Phys. Rev. Lett.* **2001**, 86, 268.

[5] F. Wilczek, *Nat. Phys.* **2009**, 5, 614.

[6] A. Kitaev, *Ann. Phys.* **2003**, 303, 2.

[7] C. Nayak, S. H. Simon, A. Stern, M. Freedman, S. Das Sarma, *Rev. Mod. Phys.* **2008**, 80, 1083.

[8] L. Fu, C. L. Kane, *Phys. Rev. Lett.* **2008**, 100, 096407.

[9] M. Z. Hasan, C. L. Kane, *Rev. Mod. Phys.* **2010**, 82, 3045.

[10] Y. Ando, *J. Phys. Soc. Jpn.* **2013**, 82, 102001.

[11] Y. S. Hor, A. J. Williams, J. G. Checkelsky, P. Roushan, J. Seo, Q. Xu, H. W. Zandbergen, A. Yazdani, N. P. Ong, R. J. Cava, *Phys. Rev. Lett.* **2010**, 104, 057001.

[12] M. Kriener, K. Segawa, Z. Ren, S. Sasaki, Y. Ando, *Phys. Rev. Lett.* **2011**, 106, 127004.

[13] Z. H. Liu, X. Yao, J. F. Shao, M. Zuo, L. Po, S. Tan, C. J. Zhang, Y. H. Zhang, *J. Am. Chem. Soc.* **2015**, 137, 10512.

[14] S. V. K. Maurya, P. Neha, P. Srivastava, S. Patnaik, *Phys. Rev. B* 2015, 92, 020506.

[15] B. J. Lawson, P. Corbae, G. Li, F. Yu, T. Asaba, C. Tinsman, Y. Qiu, J. E. Medvedeva, Y. S. Hor, L. Li, *Phys. Rev. B* **2016**, 94, 041114.

[16] M. P. Smylie, H. Claus, U. Welp, W. K. Kwok, Y. Qiu, Y. S. Hor, A. Snezhko, *Phys. Rev. B* **2016**, 94, 180510.

[17] L. Fu, E. Berg, *Phys. Rev. Lett.* **2010**, 105, 097001.

[18] S. Sasaki, M. Kriener, K. Segawa, K. Yada, Y. Tanaka, M. Sato, Y. Ando, *Phys. Rev. Lett.* **2011**, 107, 217001.

[19] N. Levy, T. Zhang, J. Ha, F. Sharifi, A. Alec Talin, Y. Kuk, J. A. Stroscio, *Phys. Rev. Lett.* **2013**, 110, 117001.

[20] G. Du, J. Shao, X. Yang, Z. Du, D. Fang, J. Wang, K. Ran, J. Wen, C. Zhang, H. Yang, Y. H. Zhang, H. H. Wen, *Nat. Commun.* **2017**, 8, 14466.

[21] T. Mizushima, A. Yamakage, M. Sato, Y. Tanaka, *Phys. Rev. B* **2014**, 90, 184516.

[22] E. Lahoud, E. Maniv, M. Shaviv Petrushevsky, M. Naamneh, A. Ribak, S. Wiedmann, L. Petaccia, Z. Salman, K. B. Chashka, Y. Dagan, A. Kanigel, *Phys. Rev. B* **2013**, 88, 195107.

[23] M. X. Wang, C. H. Liu, J. P. Xu, F. Yang, L. Miao, M. Y. Yao, C. L. Gao, C. Shen, X. C. Ma, X. Chen, Z. A. Xu, Y. Liu, S. C. Zhang, D. Qian, J. F. Jia, Q. K. Xue, *Science* **2012**, 336, 52.

[24] J. P. Xu, C. H. Liu, M. X. Wang, J. F. Ge, Z. L. Liu, X. J. Yang, Y. Chen, Y. Liu, Z. A. Xu, C. L. Gao, D. Qian, F. C. Zhang, J. F. Jia, *Phys. Rev. Lett.* **2014**, 112, 217001.

[25] J. P. Xu, M. X. Wang, Z. L. Liu, J. F. Ge, X. J. Yang, C. H. Liu, Z. A. Xu, D. D. Guan, C. L. Gao, D. Qian, Y. Liu, Q. H. Wang, F. C. Zhang, Q. K. Xue, J. F. Jia, *Phys. Rev. Lett.* **2015**, 114, 017001.

[26] H. H. Sun, K. W. Zhang, L. H. Hu, C. Li, G. Y. Wang, H. Y. Ma, Z. A. Xu, C. L. Gao, D. D. Guan, Y. Y. Li, C. H. Liu, D. Qian, Y. Zhou, L. Fu, S. C. Li, F. C. Zhang, J. F. Jia, *Phys. Rev. Lett.* **2016**, 116, 257003.

[27] L. Fu, *Phys. Rev. Lett.* **2011**, 106, 106802.

[28] R. J. Slager, A. Mesaros, V. Juričić, J. Zaanen, *Nat. Phys.* **2013**, 9, 98.

[29] T. H. Hsieh, H. Lin, J. W. Liu, W. H. Duan, A. Bansil, L. Fu, *Nat. Commun.* **2012**, 3, 982.

[30] Y. Tanaka, Z. Ren, T. Sato, K. Nakayama, S. Souma, T. Takahashi, K. Segawa, Y. Ando, *Nat. Phys.* **2012**, 8, 800.

[31] P. Dziawa, B. J. Kowalski, K. Dybko, R. Buczko, A. Szczerbakow, M. Szot, E. Łusakowska, T. Balasubramanian, B. M. Wojek, M. H. Berntsen, O. Tjernberg, T. Story, *Nat. Mater.* **2012**, 11, 1023.

[32] S. Y. Xu, C. Liu, N. Alidoust, M. Neupane, D. Qian, I. Belopolski, J. D. Denlinger, Y. J. Wang, H. Lin, L. A. Wray, G. Landolt, B. Slomski, J. H. Dil, A. Marcinkova, E. Morosan, Q. Gibson, R. Sankar, F. C. Chou, R. J. Cava, A. Bansil, M. Z. Hasan, *Nat. Commun.* **2012**, 3, 1192.

[33] C. Fang, M. J. Gilbert, B. A. Bernevig, *Phys. Rev. Lett.* **2014**, 112, 106401.

[34] X. J. Liu, J. J. He, K. T. Law, *Phys. Rev. B* **2014**, 90, 235141.

[35] S. Sasaki, Z. Ren, A. A. Taskin, K. Segawa, L. Fu, Y. Ando, *Phys. Rev. Lett.* **2012**, 109, 217004.

[36] R. Klett, J. Schönle, A. Becker, D. Dyck, K. Borisov, K. Rott, D. Ramermann, B. Büker, J. Haskenhoff, J. Krieft, T. Hübner, O. Reimer, C. Shekhar, J. M. Schmalhorst, A. Hütten, C. Felser, W. Wernsdorfer, G. Reiss, *Nano Lett.* **2018**, 18, 1264.

[37] R. A. Snyder, C. J. Trimble, C. C. Rong, P. A. Folkes, P. J. Taylor, J. R. Williams, *Phys. Rev. Lett.* **2018**, 121, 097701.

[38] G. Du, Z. Du, D. Fang, H. Yang, R. D. Zhong, J. Schneeloch, G. D. Gu, H. H. Wen, *Phys. Rev. B* **2015**, 92, 020512.

[39] T. Hashimoto, K. Yada, M. Sato, Y. Tanaka, *Phys. Rev. B* **2015**, 92, 174527.

[40] D. Zhang, H. Baek, J. Ha, T. Zhang, J. Wyrick, A. V. Davydov, Y. Kuk, J. A. Stroscio, *Phys. Rev. B* **2014**, 89, 245445.

[41] K.Oura, V. G. Lifshits, A. A. Saranin, A.V. Zotov, M. Katayama, *Surface Science*, Springer-Verlag, Berlin, Germany **2003**.

[42] V. L. Deringer, R. Dronskowski, *ChemPhysChem* **2013**, 14, 3108.

[43] C. Bombis, A. Emundts, M. Nowicki, H.P. Bonzel, *Surf. Sci.* **2002**, 511, 83.

[44] Y. Liu, D. Liang, L. Zhang, *J. Electron. Mater.* **2010**, 39, 246.

[45] A. Walsh, G. W. Watson, *J. Phys. Chem. B* **2005**, 109, 18868.

[46] N. Wang, D. West, J. W. Liu, J. Li, Q. Yan, B. L. Gu, S. B. Zhang, W. H. Duan, *Phys. Rev. B* **2014**, 89, 045142.

[47] Y. Tanaka, T. Sato, K. Nakayama, S. Souma, T. Takahashi, Z. Ren, M. Novak, K. Segawa, Y. Ando, *Phys. Rev. B* **2013**, 87, 155105.

[48] K. J. Franke, G. Schulze, J. I. Pascual, *Science* **2011**, 332, 940.

[49] J. Brand, S. Gozdzik, N. Néel, J. L. Lado, J. Fernández-Rossier, J. Kröger, *Phys. Rev. B* **2018**, 97, 195429.

[50] J. Kim, V. Chua, G. A. Fiete, H. Nam, A. H. MacDonald, C. K. Shih, *Nat. Phys.* **2012**, 8, 464.

[51] V. Cherkez, J. C. Cuevas, C. Brun, T. Cren, G. Ménard, F. Debontridder, V. S. Stolyarov, D. Roditchev, *Phys. Rev. X* **2014**, 4, 011033.

[52] S. Chi, R. Aluru, S. Grothe, A. Kreisel, U. R. Singh, B. M. Andersen, W. N. Hardy, R. Liang, D. A. Bonn, S. A. Burke, P. Wahl, *Nat. Commun.* **2017**, 8, 15996.

[53] N. Hatter, B. W. Heinrich, D. Rolf and K. J. Franke, *Nat. Commun.* **2017**, 8, 2016.

[54] R. D. Zhong, J. A. Schneeloch, T. S. Liu, F. E. Camino, J. M. Tranquada, G. D. Gu, *Phys. Rev. B* **2014**, 90, 020505.

[55] B. Voigtländer, *Scanning Probe Microscopy*, Springer-Verlag, Berlin, Germany **2015**.

[56] A. Gyenis, I. K. Drozdov, S. Nadj-Perge, O. B. Jeong, J. Seo, I. Pletikosic, T. Valla, G. D. Gu, A. Yazdani, *Phys. Rev. B* **2013**, 88, 125414.

[57] I. Zeljkovic, Y. Okada, C. Y. Huang, R. Sankar, D. Walkup, W. Zhou, M. Serbyn, F. Chou, W. F. Tsai, H. Lin, A. Bansil, L. Fu, M. Z. Hasan, V. Madhavan, *Nat. Phys.* **2014**, 10, 572.

[58] E. Abramof, S. O. Ferreira, P. H. O. Rappl, H. Closs, I. N. Bandeira, *J. Appl. Phys.* **1997**, 82, 2405.

[59] K. W. Nill, A. R. Calawa, T. C. Harman, J. N. Walpole, *Appl. Phys. Lett.* **1970**, 16, 375.

[60] J. N. Walpole, K. W. Nill, *J. Appl. Phys.* **1971**, 42, 5609.

[61] J. Baars, D. Bassett, M. Schulz, *Phys. Status Solidi A* **1978**, 49, 483.

[62] K. Takasaki, S. Tanaka, *Phys. Status Solidi A* **1977**, 40, 173.

[63] J. O. Dimmock, I. Melngailis, A. J. Strauss, *Phys. Rev. Lett.* **1966**, 16, 1193.

[64] J. R. Dixon, R. F. Bis, *Phys. Rev.* **1968**, 176, 942.

[65] E. Lahoud, E. Maniv, M. Shaviv Petrushevsky, M. Naamneh, A. Ribak, S. Wiedmann, L. Petaccia, Z. Salman, K. B. Chashka, Y. Dagan, A. Kanigel, *Phys. Rev. B* **2013**, 88, 195107.

[66] C. Zhang, X. G. He, H. Chi, R. Zhong, W. Ku, G. Gu, J. M. Tranquada, Q. Li, *Phys. Rev. B* **2018**, 98, 054503.

[67] Q. Fan, W. H. Zhang, X. Liu, Y. J. Yan, M. Q. Ren, R. Peng, H. C. Xu, B. P. Xie, J. P. Hu, T. Zhang, D. L. Feng, *Nat. Phys.* **2015**, 11, 946.

[68] Y. J. Yan, W. H. Zhang, M. Q. Ren, X. Liu, X. F. Lu, N. Z. Wang, X. H. Niu, Q. Fan, J. Miao, R. Tao, B. P. Xie, X. H. Chen, T. Zhang, D. L. Feng, *Phys. Rev. B* **2016**, 94, 134502.

[69] K. Iwaya, Y. Kohsaka, K. Okawa, T. Machida, M.S. Bahramy, T. Hanaguri, T. Sasagawa, *Nat. Commun.* **2017**, 8, 976.

[70] P. Zareapour, A. Hayat, S. Y. F. Zhao, M. Kreshchuk, A. Jain, D. C. Kwok, N. Lee, S. W. Cheong, Z. Xu, A. Yang, G. D. Gu, S. Jia, R. J. Cava, K. S. Burch, *Nat. Commun.* **2012**, 3, 1056.

[71] E. Wang, H. Ding, A. V. Fedorov, W. Yao, Z. Li, Y. F. Lv, K. Zhao, L. G. Zhang, Z. Xu, J. Schneeloch, R. Zhong, S. H. Ji, L. L. Wang, K. He, X. C. Ma, G. D. Gu, H. Yao, Q. K. Xue, X. Chen, S. Y. Zhou, *Nat. Phys.* **2013**, 9, 620.

[72] Q. L. He, H. Liu, M. He, Y. H. Lai, H. He, G. Wang, K. T. Law, R. Lortz, J. Wang, I. K. Sou, *Nat. Commun.* **2014**, 5, 4247.

[73] P. Zhang, K. Yaji, T. Hashimoto, Y. Ota, T. Kondo, K. Okazaki, Z. Wang, J. Wen, G. D. Gu, H. Ding, S. Shin, *Science* **2018**, 360, 182.

[74] D. Wang, L. Kong, P. Fan, H. Chen, S. Zhu, W. Liu, L. Cao, Y. Sun, S. Du, J. Schneeloch, R. Zhong, G. D. Gu, L. Fu, H. Ding, H. J. Gao, *Science* **2018**, 362, 333.

[75] T. Machida, Y. Sun, S. Pyon, S. Takeda, Y. Kohsaka, T. Hanaguri, T. Sasagawa, T. Tamegai, *Nat. Mater.* **2019**, 18, 811.

[76] M. J. Gray, J. Freudenstein, S. Y. F. Zhao, R. O'Connor, S. Jenkins, N. Kumar, M. Hoek, A. Kopec, S. Huh, T. Taniguchi, K. Watanabe, R. Zhong, C. Kim, G. D. Gu, K. S. Burch, *Nano Lett.* **2019**, 19, 4890.

[77] F. Qu, F. Yang, J. Shen, Y. Ding, J. Chen, Z. Ji, G. Liu, J. Fan, X. Jing, C. Yang, L. Lu, *Sci. Rep.* **2012**, 2, 339.

[78] C. J. Trimble, M. T. Wei, N. F. Q. Yuan, S. S. Kalantre, P. Liu, J. J. Cha, L. Fu, J. R. Williams, Preprint at https://arxiv.org/abs/1907.04199, **2019**.

[79] Y. Y. Li, M. X. Chen, M. Weinert, L. Li, *Nat. Commun.* **2014**, 5, 4311.

[80] Y. Y. Li, M. X. Chen, M. Weinert, L. Li, *2D Mater.* **2019**, 6, 025038.

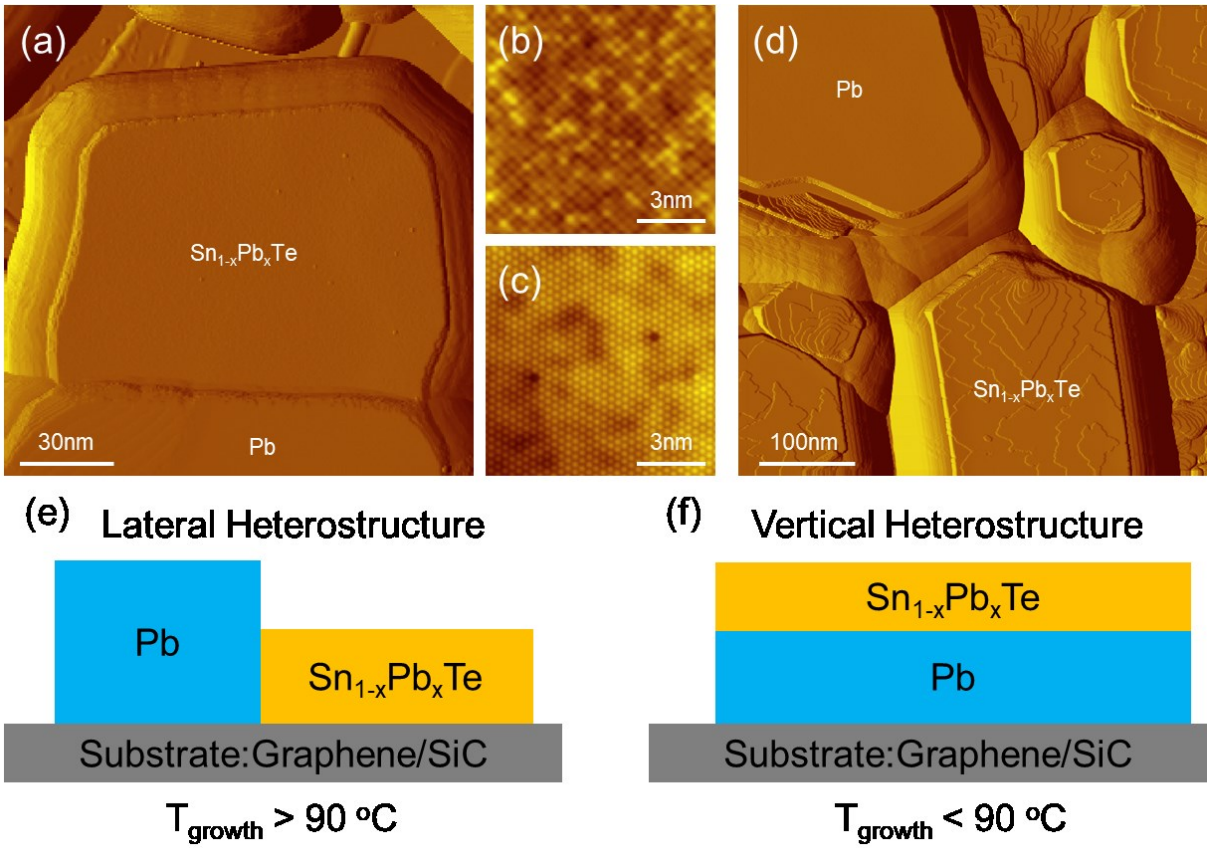

Figure 1. MBE growth of lateral and vertical $Sn_{1-x}Pb_xTe$-Pb heterostructures. a) STM topography of a lateral $Sn_{1-x}Pb_xTe$-Pb heterostructure. b,c) Atomically resolved STM images of $Sn_{1-x}Pb_xTe$ (001) (b) (V_s = 1.0 V, I_t = 0.15 nA) and Pb (111) (c) (V_s = -0.041 V, I_t = 0.23 nA) taken on other lateral heterostructures. d) STM topography of a vertical $Sn_{1-x}Pb_xTe$-Pb heterostructure. e,f) Schematic diagrams of the lateral (e) and vertical (f) $Sn_{1-x}Pb_xTe$-Pb heterostructures.

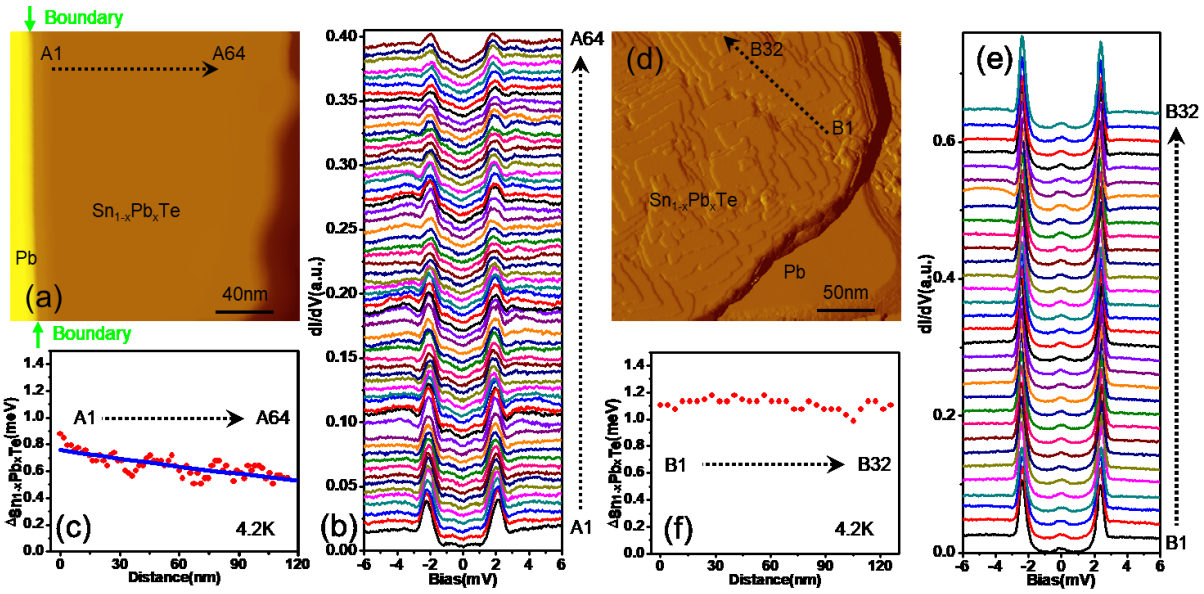

Figure 2. Proximity effects on lateral and vertical $Sn_{1-x}Pb_xTe$-Pb heterostructures. a) STM topography of a lateral $Sn_{1-x}Pb_xTe$-Pb heterostructure. The thicknesses of the $Sn_{1-x}Pb_xTe$ island and the Pb island are 9.7 nm (31 ML) and 16.3 nm (57 ML) respectively. b) Series of d*I*/d*V* spectra measured at 4.2 K along the black dashed line in (a). c) Spatial evolution of $\Delta_{Sn1-xPbxTe}$ as a function of distance. The solid blue line is an exponential fit with a decay length L = 362 nm. A1 is at the distance of ~10 nm away from the Pb island edge marked by green arrows. d) STM topography of a vertical $Sn_{1-x}Pb_xTe$-Pb heterostructure. The thicknesses of the $Sn_{1-x}Pb_xTe$ island is ~ 15 nm (~ 48 ML). e) Series of dI/dV spectra measured at 4.2 K along the black dashed line in (d). f) Spatial evolution of $\Delta_{Sn1-xPbxTe}$ as a function of distance. The setpoints for the d*I*/d*V* measurement are V_s = 10 mV, I_t = 0.1 nA.

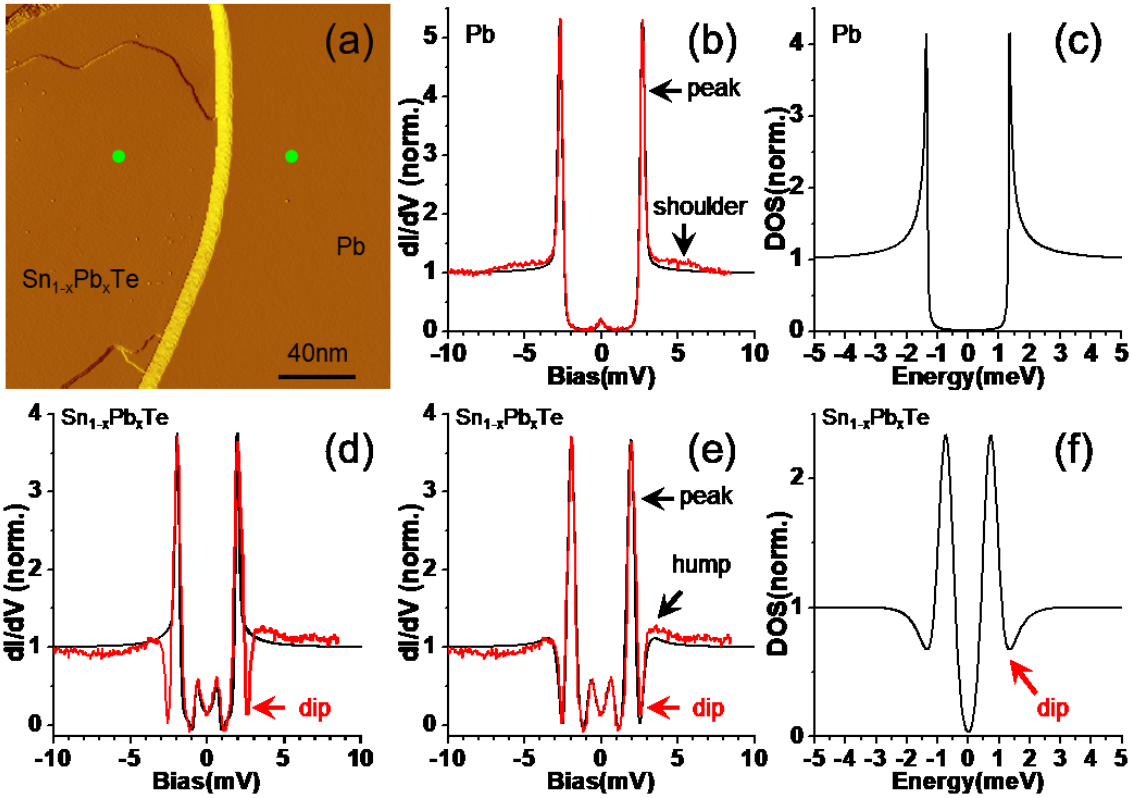

Figure 3. Unconventional proximity-induced superconductivity of $Sn_{1-x}Pb_xTe$. a) STM topography of a lateral $Sn_{1-x}Pb_xTe$-Pb heterostructure. The Pb island is 5.5 nm higher than the $Sn_{1-x}Pb_xTe$ island. b) d*I*/d*V* spectrum (red curve) taken on the Pb island at the position shown in (a). The black curve is the simulated one. c) Corresponding sample DOS of Pb. The parameters are $\Delta_t = \Delta_s = 1.33$ meV, $\Gamma_t = \Gamma_s = 0.025$ meV, $w = 0.19$ meV. d) d*I*/d*V* spectrum (red curve) taken on the $Sn_{1-x}Pb_xTe$ island at the position shown in (a). The black curve is the simulated one with a BCS-like sample DOS. The parameters are $\Delta_t = 1.35$ meV, $\Delta_s = 0.58$ meV, $\Gamma_t = \Gamma_s = 0.025$ meV, $w = 0.15$ meV. e) The same d*I*/d*V* spectrum (red curve) shown in (d). The black curve is the simulated one with a modified sample DOS. The parameters are $\Delta_t = 1.33$ meV, $\Gamma_t = 0.025$ meV, $\Delta_{s1} = 0.72$ meV, $\Gamma_{s1} = 0.34$ meV, $\Delta_{s2} = 1.20$ meV, $\Gamma_{s2} = 0.30$ meV, $w = 0.19$ meV. f) Corresponding sample DOS of $Sn_{1-x}Pb_xTe$. The setpoints for the d*I*/d*V* measurement are $V_s = 10$ mV, $I_t = 0.1$ nA.

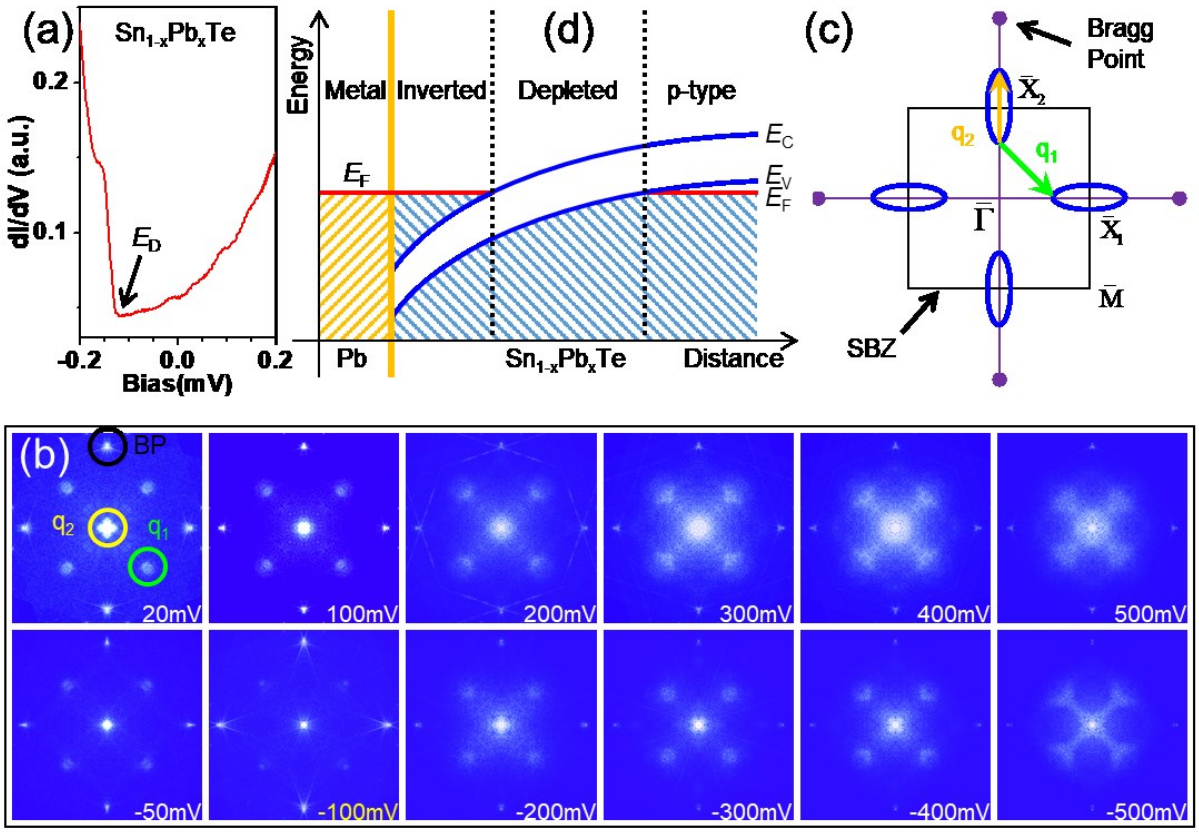

Figure 4. QPI patterns taken on $Sn_{1-x}Pb_xTe$ (001). a) Typical d*I*/d*V* spectrum taken on the $Sn_{1-x}Pb_xTe$ region of a lateral $Sn_{1-x}Pb_xTe$-Pb heterostructure. b) Symmetrized FT of d*I*/d*V* maps taken over a 50×50 nm^2 area at various sample bias voltages (I_t = 0.1 nA). c) Schematic Fermi surface of $Sn_{1-x}Pb_xTe$ (001) in the SBZ. d) Energy diagram for the lateral $Sn_{1-x}Pb_xTe$-Pb heterostructure.

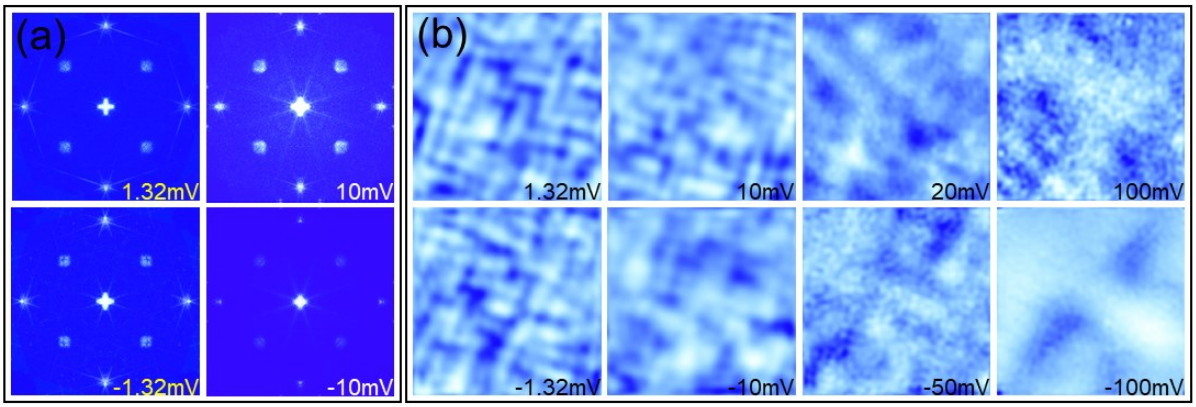

Figure 5. Comparison of QPI patterns inside and outside the superconducting gap of $Sn_{1-x}Pb_xTe$. (a) Symmetrized FT of d*I*/d*V* maps around E_F. (b) QPI in real space (50×50 nm^2) induced by intra-pocket scattering $\boldsymbol{q}_2$.

Superconducting topological crystalline insulators are expected to form a new type of topological superconductors protected by lattice symmetries. Unconventional peak-dip-hump gap features and fourfold symmetric quasiparticle interference patterns taken at the zero energy support the presence of the topological superconductivity in $Sn_{1-x}Pb_xTe$-Pb heterostructures. Moreover, the superconducting proximity effect is found to be unexpectedly strong even at 4.2 K.

Keyword: superconducting topological material

Hao Yang, Yao-Yi Li*, Teng-Teng Liu, Huan-Yi Xue, Dan-Dan Guan, Shi-Yong Wang, Hao Zheng, Can-Hua Liu, Liang Fu, and Jin-Feng Jia*

Superconductivity of Topological Surface States and Strong Proximity Effect in $Sn_{1-x}Pb_xTe$-Pb Heterostructures